

VIP Very Important Paper



# Sodium Quasi-Intercalation in Black P for Superior Sodium-Ion Battery Anodes

Tae-Hyun Kim<sup>[a, b]</sup> and Cheol-Min Park<sup>\*[a, b]</sup>

Herein, a Na quasi-intercalation concept in black P is developed in order to achieve superior P-based Na-ion battery (NIB) anodes. Firstly, black P with a puckered layer structure is synthesized via a simple solid-state reaction using commercially available red P. Additionally, an amorphous carbon modified black P nanocomposite (black P@C) is prepared to optimize its electrochemical Na reversibility. Furthermore, the Na reaction pathways of black P are demonstrated using various *ex situ* analytical tools. During sodiation/desodiation, black P under-

goes the two-step reactions of sequential quasi-intercalation of NaP formation (at 0.25 V) and conversion of Na<sub>3</sub>P formation (at 0 V). Interestingly, black P@C shows poor cycling performance when using the conversion reaction, but it shows superior performance when using the quasi-intercalation reaction between black P and NaP. Therefore, we anticipate that the Na quasi-intercalation in black P@C will lead to high-performance NIB anodes.

## 1. Introduction

Recently, Na-ion batteries (NIBs) have received attention as an attractive alternative to Li-ion batteries (LIBs), due to abundant Na resources and the similar chemical properties between Li and Na.<sup>[1]</sup> However, while graphite is used widely as an LIB anode, it is not suitable for use as an NIB anode due to the unfavorable mismatch between Na-ion and graphite structure.<sup>[2]</sup> Other carbon-based materials, such as hard carbon,<sup>[3]</sup> amorphous carbon,<sup>[4]</sup> carbon nanotube,<sup>[5]</sup> graphene,<sup>[1c]</sup> etc., have been investigated as NIB anodes. However, they showed limited reversible capacity at less than 300 mAh g<sup>-1</sup>. Therefore, elements capable of alloying with Na, such as Ge,<sup>[6]</sup> Sn,<sup>[7]</sup> P,<sup>[8]</sup> and Sb,<sup>[9]</sup> have been proposed as possible candidates for high capacity NIB anodes because the elements can be electrochemically alloyed with large amounts of Na. Among the elements that can be alloyed with Na, P is the most promising because it can form the Na<sub>3</sub>P phase, which provides the highest theoretical capacity of 2,596 mAh g<sup>-1</sup> as NIB anodes.

Elemental P exists in the three main allotropes of white P,<sup>[10]</sup> red P,<sup>[11]</sup> and black P.<sup>[12]</sup> Among the allotropes of P, black P has attracted much attention due to the distinctive characteristics of a puckered layer structure and semiconducting properties. However, high pressure (1.2 GPa) and temperature (above 200 °C) is needed to synthesize black P, which hinders its wider application.<sup>[10]</sup> In 2007, our group first reported that black P can be synthesized using a simple solid-state reaction.<sup>[13]</sup> Since our

report, black P has been highly researched for numerous uses in optoelectronic,<sup>[14]</sup> photovoltaic,<sup>[15]</sup> electrocatalyst,<sup>[16]</sup> and semiconductor applications.<sup>[17]</sup> Additionally, the structure of orthorhombic black P consisting of multiple, two-dimensional, and puckered phosphorene layers resembles that of graphite.<sup>[13,18]</sup> Owing to its distinctive layer structure, many approaches have been investigated for its application in energy storage materials for LIB and NIB anodes. In the application of LIB anodes, although black P exhibits high capacity, it has a relatively high lithiation/delithiation voltage of ~0.8 V/~1.1 V (vs. Li<sup>+</sup>/Li) and poor cycling ability.<sup>[13,19]</sup> By contrast, black P in the application of NIB anodes exhibits a high capacity and an appropriate sodiation/desodiation voltage of ~0.2 V/~0.5 V (vs. Na<sup>+</sup>/Na), which demonstrates that black P is a more suitable anode material in NIBs.<sup>[8,20]</sup> However, a large volumetric change during cycling makes it difficult for black P to maintain stable cycling ability in NIB anodes. Additionally, several studies have detailed the electrochemical Na reaction pathways of black P as NIB anodes, but further analyses are required in order to fully understand the exact Na reaction pathway mechanism. Therefore, the enhancement of cycling performance and an understanding of the electrochemical Na reaction pathways are essential for the commercial application of black P as NIB anodes.

In this study, black P was synthesized using a simple solid-state reaction as referenced in our previous report.<sup>[13]</sup> To optimize its electrochemical Na reversibility, an amorphous carbon modified black P nanocomposite (black P@C) was also prepared. Furthermore, the electrochemical Na reaction pathways of black P were thoroughly demonstrated using various *ex situ* analytical tools. Based on the results of the Na reaction pathways, a concept of Na quasi-intercalation in black P is suggested as a promising solution for high-performance black P-based Na-ion battery anodes.

[a] T.-H. Kim, Prof. C.-M. Park  
School of Material Science and Engineering  
Kumoh National Institute of Technology  
Gumi, Gyeongbuk 39177 (Republic of Korea)  
E-mail: cmpark@kumoh.ac.kr

[b] T.-H. Kim, Prof. C.-M. Park  
Department of Energy Engineering Convergence  
Kumoh National Institute of Technology  
Gumi, Gyeongbuk 39177 (Republic of Korea)

 Supporting information for this article is available on the WWW under  
<https://doi.org/10.1002/batt.202000188>

## 2. Results and Discussion

To compare the structural characteristics of red P, black P, and black P@C, X-ray powder diffraction (XRD) with color photo image, Raman spectroscopy, solid-state nuclear magnetic resonance spectroscopy (NMR), and high-resolution transmission electron microscopy (HRTEM) were conducted and their results are shown in Figure 1a, b, c, and d-f, respectively. Red P is displayed in red color and its crystal structure has an amorphous nature with two broad humps at 12–18 and 26–38 degrees (i in Figure 1a). By contrast, the XRD pattern of the synthesized black P corresponded well to the standard of the black P phase (JCPDS #76-1957) and its color was transformed to black (ii in Figure 1a). All XRD peaks of the black P@C also corresponded well to the black P with reduced crystallinity (iii in Figure 1a), which confirms that the composite comprising of black P and amorphous carbon was well prepared. The Raman signature of the amorphous red P is consistent with those of previous reports (i in Figure 1b).<sup>[8a,b]</sup> The black P had three main Raman bands at 458, 427, and 355 cm<sup>-1</sup>, assigned to A<sub>g</sub><sup>2</sup>, B<sub>2g</sub>, and A<sub>g</sub><sup>1</sup> (ii in Figure 1b), respectively, which are the typical Raman fingerprints of black P.<sup>[8a,b]</sup> A tiny Raman hump at ~900 cm<sup>-1</sup> in red P and black P was attributed to P—O—P

bridges originating from slight oxidation.<sup>[21]</sup> Additionally, these Raman results are consistent with those for black P@C (iii in Figure 1b) and the Raman peaks in the region of 1200~1700 cm<sup>-1</sup> originated from the D and G bands of amorphous carbon. The <sup>31</sup>P MAS NMR spectrum of red P contained a broad peak at approximately +54 ppm (i in Figure 1c). By contrast, the <sup>31</sup>P MAS NMR spectra of black P and black P@C both contained the same sharp peak at +18 ppm (ii and iii in Figure 1c), and the chemical shift was in agreement with that of a previously reported black P NMR spectrum.<sup>[8b]</sup> Figure 1d-f shows the HRTEM images with the corresponding diffraction patterns (DPs) of red P, black P, and black P@C. Although red P is typically amorphous without a clear ring pattern (Figure 1d), black P has definite polycrystalline ring patterns of (020), (021), (111), (131), and (151) planes (Figure 1e), which coincides well with the orthorhombic black P phase. The composite of black P@C consisted of nanocrystalline black P (approximately 5–10 nm size) within the amorphous carbon matrices (Figure 1f). Furthermore, the images of the scanning TEM and corresponding energy-dispersive X-ray spectroscopy (EDX) mapping (red: black P, blue: amorphous C) demonstrate the uniform dispersion of black P nanocrystallites within the amorphous carbon matrices (Figure 1g). The results of the scanning

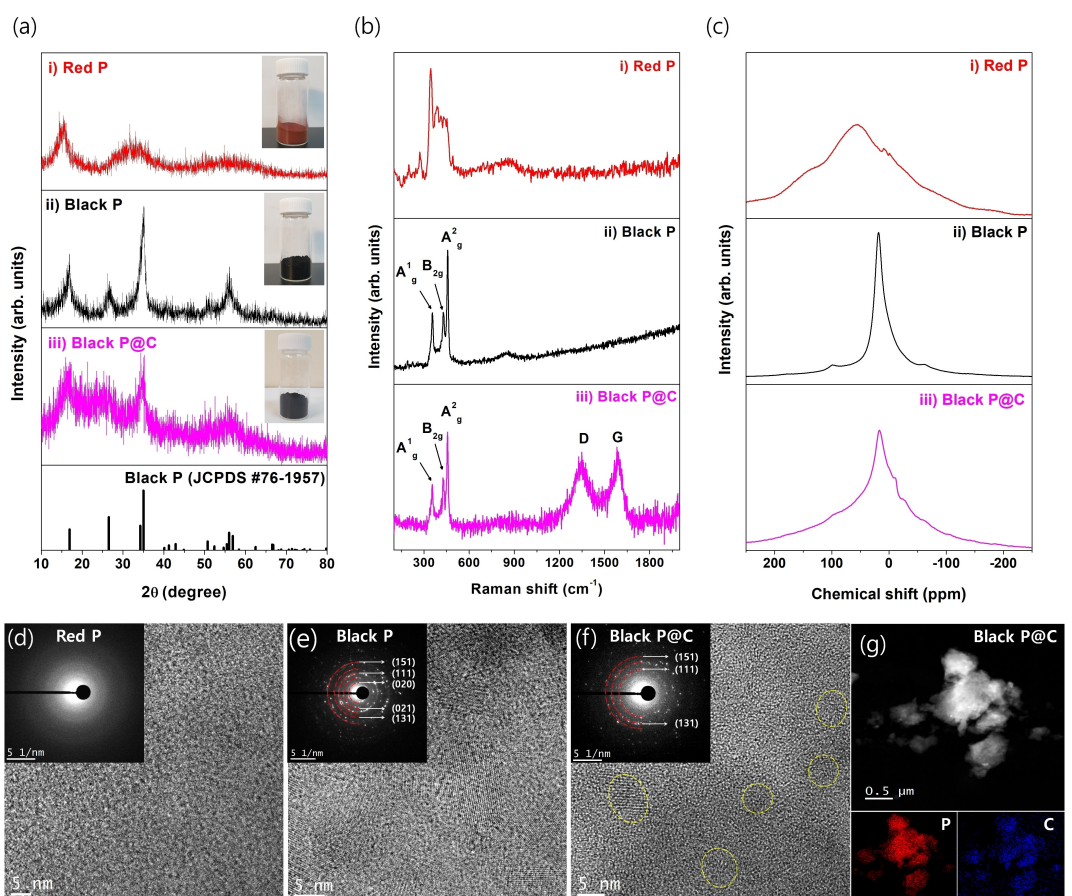


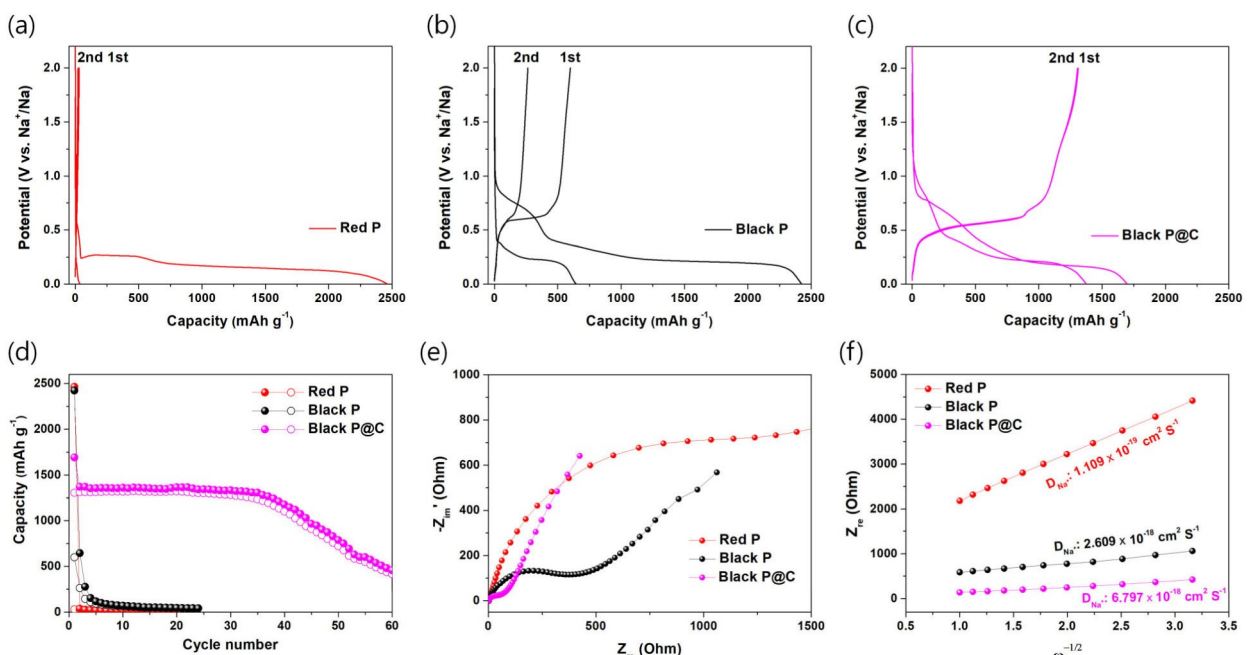
**Figure 1.** Synthesis and structural characteristics of red P, black P, and black P@C. a) XRD spectrum of i) red P, ii) black P, and iii) black P@C and black P standard (JCPDS #76-1957). b) Raman spectrum of i) red P, ii) black P, and iii) black P@C. c) <sup>31</sup>P MAS NMR spectrum of i) red P, ii) black P, and iii) black P@C. d–f) High-resolution TEM image with the corresponding DPs of d) red P, e) black P, and f) black P@C. g) Scanning TEM and corresponding EDX mappings of black P@C (red: black P, blue: amorphous C).

electron microscopy (SEM) and particle size analyzer (PSA) confirm that the mean particle size ( $D_{50}$ ) of red P, black P, and black P@C was 15.2, 5.8, and 5.0  $\mu\text{m}$ , respectively (Figure S1).

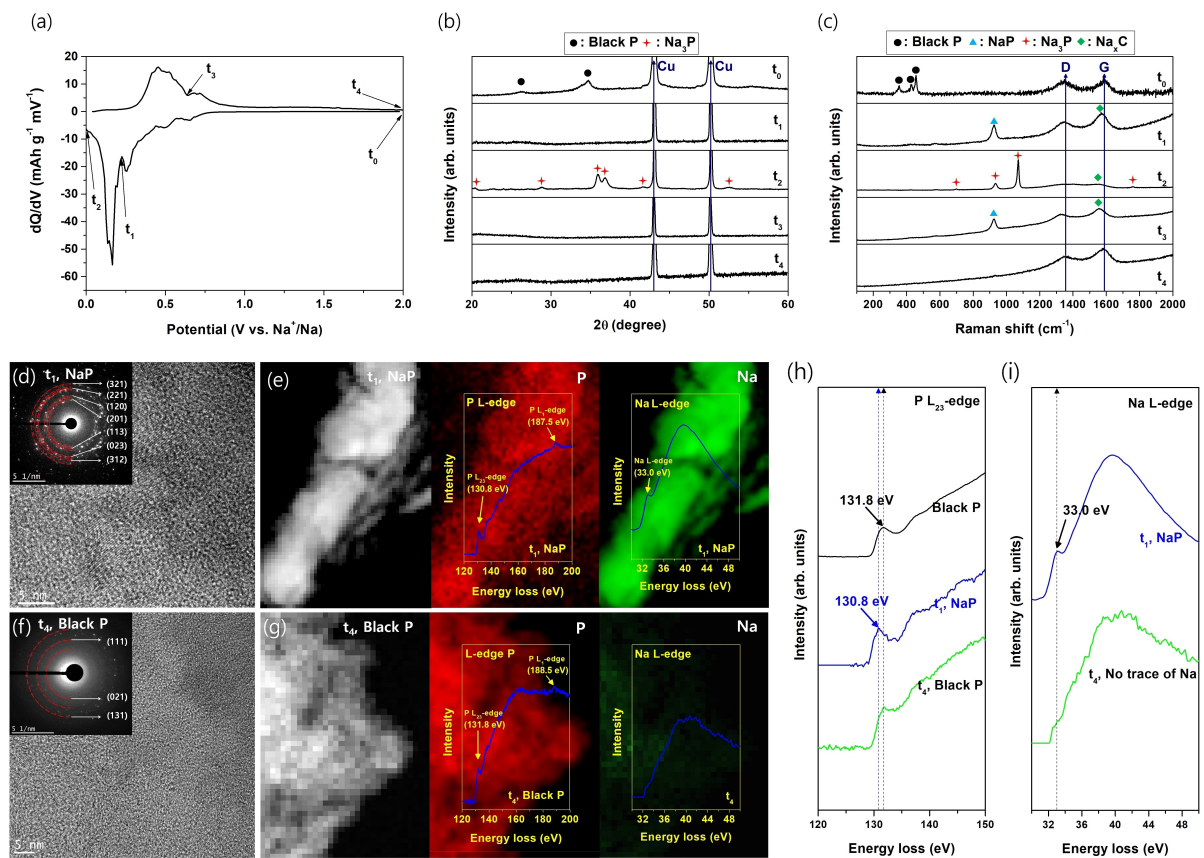
A comparison of the results of the electrochemical behavior of red P, black P, and black P@C is shown in Figures 2a–d. In the galvanostatic voltage profile of red P (current density: 50  $\text{mA g}^{-1}$ ), it demonstrated a high first sodiation capacity of 2465  $\text{mAh g}^{-1}$ , but its desodiation capacity was negligible, showing extremely poor reversibility with Na (Figure 2a). In the case of the galvanostatic voltage profile of black P (current density: 50  $\text{mA g}^{-1}$ ), it showed a similar first sodiation capacity of 2424  $\text{mAh g}^{-1}$  with red P, but its desodiation capacity was 599  $\text{mAh g}^{-1}$  (Figure 2b), which demonstrates that the Na reversibility of black P is significantly higher than that of red P. Furthermore, the galvanostatic voltage profile of black P@C (current density: 50  $\text{mA g}^{-1}$ ) demonstrated highly reversible behavior with the first sodiation/desodiation capacity of 1692/1305  $\text{mAh g}^{-1}$ , with the corresponding coulombic efficiency of 77.1% (Figure 2c). The contributed sodiation/desodiation capacity of ball milling (BM)-treated C (40 wt% composition) in the black P@C was approximately 249/83  $\text{mAh g}^{-1}$  (Figure S2). Therefore, the black P in the composite showed the sodiation values very close to its theoretical capacity, which demonstrates that the composite preparation process by BM is very useful for eliciting high Na reversibility. The comparison of the cycling ability of red P, black P, and black P@C demonstrates that red P and black P had very poor cycling ability, whereas black P@C had good cycling ability up to 35 cycles, but the capacity subsequently degraded unexpectedly (Figure 2d). The unexpected capacity degradation in black P@C confirms that the nanocomposite of black P@C was not

sustained by repetitive  $\text{Na}_3\text{P}$  phase formation/release after 35 cycles. To elucidate the Na reversible ability of red P, black P, and black P@C, the results of the electrochemical impedance (EI) spectroscopy measurements and the Na-ion diffusivity are compared in Figures 2e and f, respectively. As is known, red P shows very poor charge transfer resistance (1633  $\Omega$ ) and  $\text{Na}^+$  diffusivity ( $1.109 \times 10^{-19} \text{ cm}^2 \text{ s}^{-1}$ ), which originated from its intrinsic amorphous nature. However, the charge transfer resistance (387  $\Omega$ ) and  $\text{Na}^+$  diffusivity ( $2.609 \times 10^{-18} \text{ cm}^2 \text{ s}^{-1}$ ) of black P was significantly enhanced due to the distinctive structural characteristics of a puckered layer structure. Furthermore, the black P@C had the lowest charge transfer resistance (173  $\Omega$ ) and the highest  $\text{Na}^+$  diffusivity ( $6.797 \times 10^{-18} \text{ cm}^2 \text{ s}^{-1}$ ), which were achieved by the preparation of a composite comprising nanocrystalline black P (approximately 5–10 nm size) in the conductive carbon black matrices. These results of the EI spectroscopy and the Na-ion diffusivity demonstrate that the Na reversibility is significantly related to the electrochemical resistances of red P, black P, and black P@C.

To clarify the electrochemical Na reaction pathways of black P, various *ex situ* analyses, XRD, Raman spectroscopy, HRTEM, and electron energy loss spectroscopy (EELS), were performed on the electrodes of black P@C referenced with its first dQ/dV result (Figure 3). The first dQ/dV result confirms that black P has two peaks, consisting of a small and a large peak, during sodiation and desodiation, respectively (Figure 3a). When the open circuit voltage ( $\text{OCV}$ ,  $t_0$  in Figure 3a) was dropped to 0.25 V ( $t_1$  in Figure 3a), the characteristic peaks of XRD were not identified, which may have been due to the extreme nanocrystallization behavior of the sodiated phase in the electrode ( $t_1$  in Figure 3b). However, the Raman peak of black P@C ( $t_0$  in



**Figure 2.** Electrochemical behavior and EI spectroscopy results of red P, black P, and black P@C. a) 1st and 2nd voltage profiles of red P. b) 1st and 2nd voltage profiles of black P. c) 1st and 2nd voltage profiles of black P@C. d) Cycling ability of red P, black P, and black P@C. e) EI spectroscopy measurement results of red P, black P, and black P@C. f) Na-ion diffusivity plot of red P, black P, and black P@C.



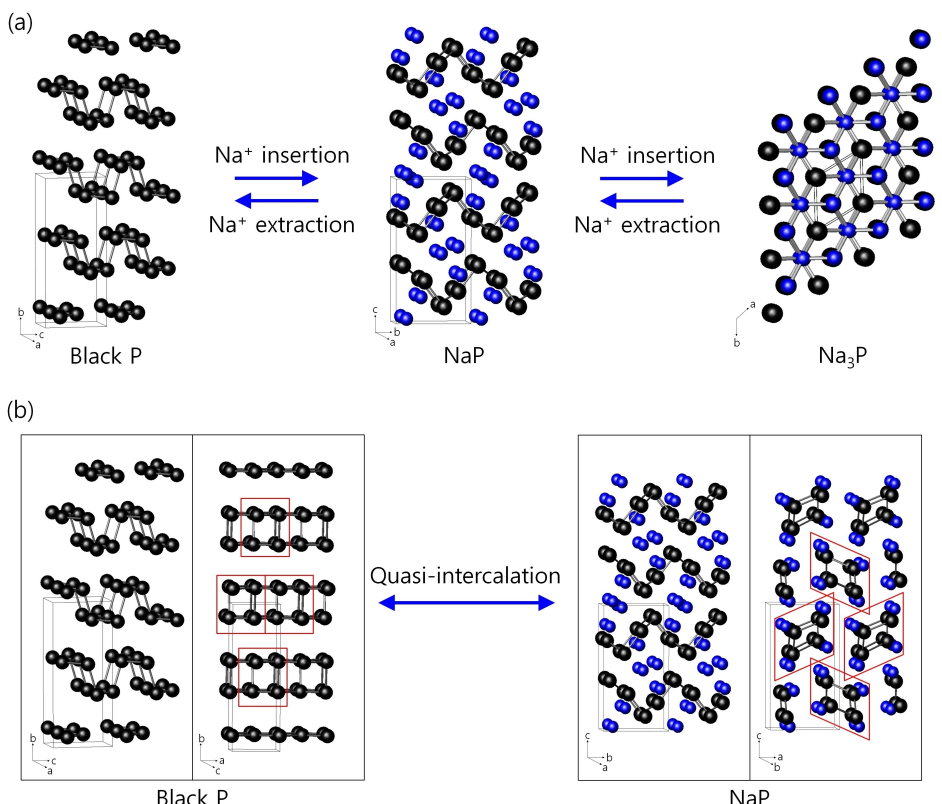
**Figure 3.** Electrochemical Na reaction pathways of black P using black P@C. a) 1st cycle  $dQ/dV$  plot of black P@C. b) *Ex situ* XRD profile during the first sodiation/desodiation of black P@C. c) *Ex situ* Raman spectra of the first sodiation/desodiation of black P@C. d) *Ex situ* HRTEM image with the corresponding lattice spacing at the sodiated state of 0.25 V. e) *Ex situ* P and Na L-edge EELS mapping images (red: black P, green: Na) at the sodiated state of 0.25 V. f) *Ex situ* HRTEM image with the corresponding lattice spacing at the desodiated state of 2 V. g) *Ex situ* P and Na L-edge EELS mapping images (red: black P, green: Na) at the desodiated state of 2 V. h) P  $L_{2,3}$ -edge EELS spectrum at pristine, sodiated (0.25 V), and desodiated (2 V) states. i) Na L-edge EELS spectrum at sodiated (0.25 V) and desodiated (2 V) states.

Figure 3c) disappeared and a significant new Raman peak ( $925\text{ cm}^{-1}$ ,  $t_1$  in Figure 3c) appeared. To confirm the Raman peak at this voltage, additional HRTEM (Figure 3d) and EELS (Figure 3e and h) analyses were performed. The results of the HRTEM image with the corresponding DPs definitely indicated the formation of an extremely small nanocrystalline NaP phase. Additionally, the P and Na L-edge EELS mapping images (red: black P, green: Na, Figure 3e) and spectrum (P  $L_{2,3}$ -edge: 130.8 eV, Figure 3h; Na L-edge: 33.0 eV, Figure 3i) also supported the formation of the NaP phase and its uniform dispersion. Furthermore, the contributed capacity of black P (60 wt% composition) in the composite corresponded well to the 1 mol Na reaction with black P. Additionally, the EDX atomic ratio of P to Na was 48.19:51.81, representing approximately 1:1 (Figure S3). When the voltage was dropped fully to 0 V ( $t_2$  in Figure 3a), the NaP was transformed to  $\text{Na}_3\text{P}$ , which was demonstrated by the results of the XRD ( $t_2$  in Figure 3b) and Raman spectroscopy ( $699\text{ cm}^{-1}$ ,  $935\text{ cm}^{-1}$ ,  $1071\text{ cm}^{-1}$ , and  $1760\text{ cm}^{-1}$ ,  $t_2$  in Figure 3c).<sup>[22]</sup> Inversely, when the voltage was raised to 0.64 V ( $t_3$  in Figure 3a), the  $\text{Na}_3\text{P}$  phase disappeared and characteristic peaks of XRD were not identified ( $t_3$  in Figure 3b). However, the Raman peak of  $925\text{ cm}^{-1}$ , corresponding to NaP, reappeared ( $t_3$  in Figure 3c). At

the full desodiated voltage of 2 V ( $t_4$  in Figure 3a), although characteristic peaks of XRD and Raman spectroscopy were not observed ( $t_4$  in Figure 3b and c), the HRTEM image with the corresponding DPs indicated recovery to an extremely small nanocrystalline black P phase (Figure 3f). Additionally, P and Na L-edge EELS mapping images (red: black P, green: Na, Figure 3g) and spectrum demonstrated that Na was almost fully extracted from the NaP phase and recovered to the black P phase (P  $L_{2,3}$ -edge: 131.8 eV, Figure 3h; no trace of Na L-edge, Figure 3i).<sup>[23]</sup> Based on the results of the various *ex situ* analyses, the following electrochemical Na reaction pathways of black P are suggested:

- Sodiation of black P in black P@C; Black P (orthorhombic)  $\rightarrow$  NaP (orthorhombic)  $\rightarrow$   $\text{Na}_3\text{P}$  (hexagonal)
- Desodiation of black P in black P@C;  $\text{Na}_3\text{P}$  (hexagonal)  $\rightarrow$  NaP (orthorhombic)  $\rightarrow$  Black P (orthorhombic)

To crystallographically study the electrochemical Na reaction pathways of black P, the transformations of the crystalline structure of black P are represented in Figure 4a. The orthorhombic black P (S. G. Cmca;  $a = 3.313\text{ \AA}$ ,  $b = 10.473\text{ \AA}$ ,  $c = 4.374\text{ \AA}$ ) has puckered 2D-phosphorene layer planes, which enable Na ions to insert and storage easily. The black P transformed into the orthorhombic NaP (S. G. P212121;  $a =$



**Figure 4.** Crystallographic representation of the Na reaction pathways of black P using black P@C. a) Electrochemical Na reaction pathways of black P during sodiation/desodiation. b) Crystallographic comparison of the quasi-intercalation behavior between orthorhombic black P and orthorhombic NaP.

$a = 6.038 \text{ \AA}$ ,  $b = 5.6430 \text{ \AA}$ ,  $c = 10.1420 \text{ \AA}$ ) at 0.25 V. Notably, the orthorhombic NaP has periodic Na arrangements within the gaps of the spiral 1D-layer chains composed of P atoms. In our previous reports, we suggested the concept of Li quasi-intercalation using the 2D-layer materials of ZnSb and grey As.<sup>[24]</sup> The Li quasi-intercalation was defined that the 2D-layer materials were transformed into periodic Li arrangements within the gaps of the other layer structures composed of host atoms during lithiation.<sup>[24]</sup> The quasi-intercalation behavior has various advantageous features; first, the small extent of deformation during cycling leads to a lower increase in volume during cycling, which results in good cycling ability. Second, the similar crystallographic relationship leads to a small electrochemical recrystallization energy, which contributes to the fast rate-capability. Glushenkov's group also suggested that it could improve the electrochemical performance of black P in restricted potential windows (vs. Li<sup>+</sup>/Li and Na<sup>+</sup>/Na).<sup>[8b]</sup> Interestingly, the Na quasi-intercalation behavior between black P and NaP is possible in view of crystallography, as shown in Figure 4b. During sodiation, the puckered 2D-layer planes of black P transform into periodic Na arrangements within the gaps of the spiral 1D-layer chains composed of P atoms through the cleavage along the c-axis and slight distortion by reconstruction, which can reduce volume deformation and electrochemical recrystallization energy and contribute to enhanced electrochemical performance.

To confirm the electrochemical performance when using the quasi-intercalation reaction between black P and NaP, the voltage profiles of black P@C within the range of 0.25 V (corresponding to NaP)–2 V (corresponding to black P) are shown in Figure 5a. The quasi-intercalation behavior of black P@C resulted in high first reversible capacity of  $532 \text{ mAh g}^{-1}$ , which was maintained well after 100 cycles almost no capacity decrease. To observe the excellent capacity retention ability of quasi-intercalation of black P@C, swelling variation of black P and black P@C electrodes during sodiation/desodiation was tested (Figure 5b and S4). The thickness of black P and black P@C electrodes at the full sodiated voltage of 0 V (corresponding to Na<sub>3</sub>P) increased to 149% and 80% of initial thickness, respectively, and they decreased to 116% and 19% of initial thickness at the full desodiated voltage of 2 V, respectively, which explains that the preparation of a composite modified with carbon effectively alleviates the volume increase of black P. Notably, when using the quasi-intercalation reaction between black P and NaP within the voltage range of 0.25 V (corresponding to NaP)–2 V (corresponding to black P), the electrode thickness of black P and black P@C significantly reduced to 36% and 16% of initial thickness at the sodiated voltage of 0.25 V, respectively, and 17% and 9% of initial thickness at the desodiated voltage of 2 V, respectively, which demonstrates that the Na quasi-intercalation behavior is a very effective alternative approach to reduce large variation in volume of P-based anodes. Additionally, the morphological

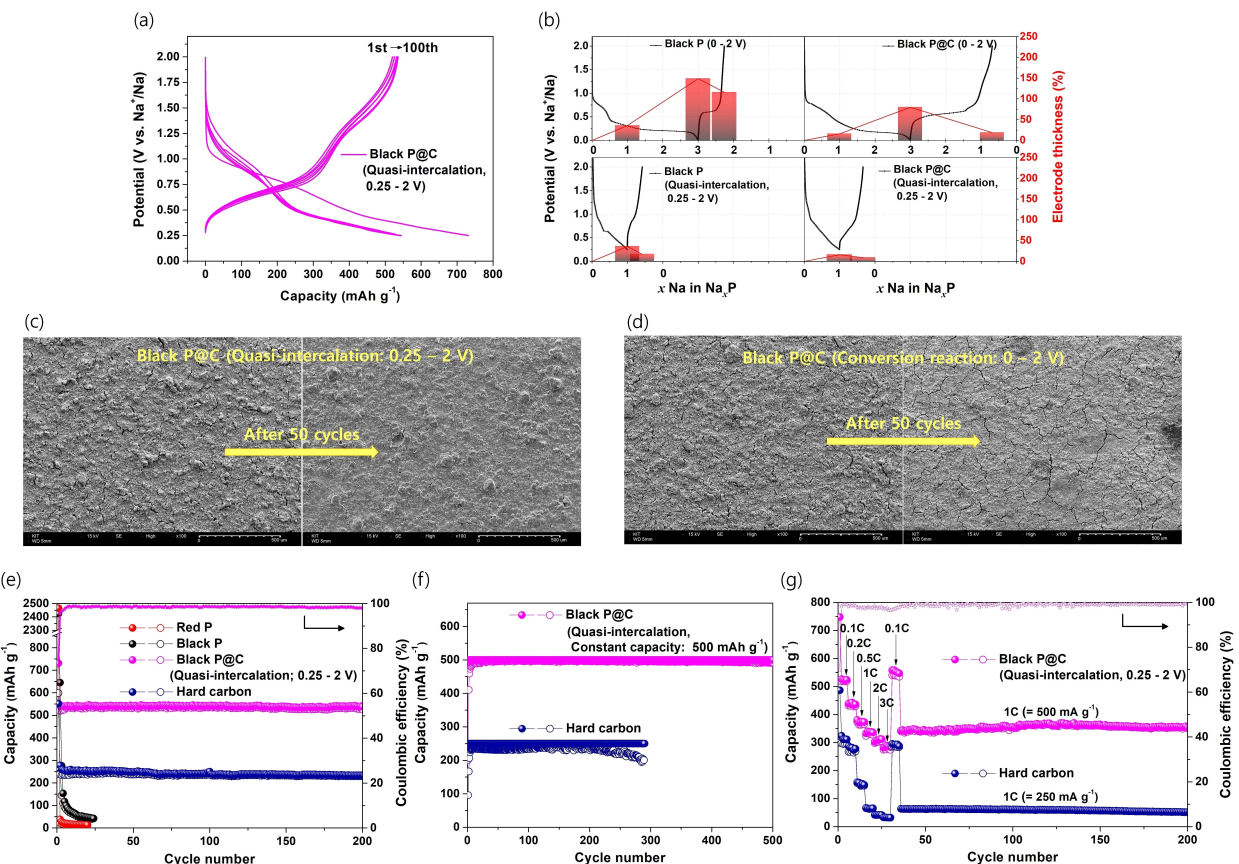


**Figure 5.** Electrochemical performance of the black P@C using the quasi-intercalation reaction. a) Voltage profiles of black P@C using the quasi-intercalation reaction (current density:  $50 \text{ mA g}^{-1}$ , voltage range:  $0.25\text{--}2 \text{ V}$ ). b) Electrode thickness change of black P and black P@C using the conversion reaction (voltage range:  $0\text{--}2 \text{ V}$ ) and quasi-intercalation reaction (voltage range:  $0.25\text{--}2 \text{ V}$ ). c) *Ex-situ* SEM results of the black P@C electrode using a quasi-intercalation ( $0.25\text{--}2 \text{ V}$ ) before cycling and after 50 cycles. d) *Ex-situ* SEM results of the black P@C electrode without a quasi-intercalation ( $0\text{--}2 \text{ V}$ ) before cycling and after 50 cycles. e) Cycling ability at cycling rate  $50 \text{ mA g}^{-1}$  of red P, black P, black P@C (using quasi-intercalation), and hard carbon. f) Cycling ability at constant capacity for black P@C (constant capacity:  $500 \text{ mAh g}^{-1}$ , cycling rate:  $50 \text{ mA g}^{-1}$ ) and hard carbon (constant capacity:  $250 \text{ mAh g}^{-1}$ , cycling rate:  $50 \text{ mA g}^{-1}$ ). g) Comparison of rate-capabilities for black P@C (rate of  $1 \text{ C}$ ,  $500 \text{ mA g}^{-1}$ ) and hard carbon (rate of  $1 \text{ C}$ ,  $250 \text{ mA g}^{-1}$ ).

observation using *ex situ* SEM of the black P@C electrodes also demonstrates that the Na quasi-intercalation in black P (voltage range:  $0.25\text{--}2 \text{ V}$ , Figure 5c) leads to a significant reduction in volume fluctuation compared to the electrodes used in the conversion reaction (voltage range:  $0\text{--}2 \text{ V}$ , Figure 5d). Due to the Na quasi-intercalation in black P@C, it had a superior capacity retention of 99.1% with a highly reversible capacity of  $527 \text{ mAh g}^{-1}$  after 200 cycles (voltage range:  $0.25\text{--}2 \text{ V}$ , cycling rate:  $50 \text{ mA g}^{-1}$ ) compared to those of the hard carbon anode (voltage range:  $0\text{--}2 \text{ V}$ , cycling rate:  $50 \text{ mA g}^{-1}$ ; first reversible capacity:  $240 \text{ mAh g}^{-1}$ ; capacity retention after 200 cycles: 95.8%) as shown in Figure 5e. Furthermore, the quasi-intercalation behavior of black P@C resulted in excellent cycling ability above 500 cycles at the constant capacity of  $500 \text{ mAh g}^{-1}$ , which is also better than that of hard carbon anode (Figure 5f). Notably, the excellent cycling ability above 500 cycles with the reversible capacity of  $500 \text{ mAh g}^{-1}$  is one of the highest values reported among P-based anode materials for NIBs.<sup>[8,20]</sup> The Na quasi-intercalation behavior in black P@C also contributed to the fast rate-capability (Figure 5g). At the fast rates of  $1 \text{ C}$  ( $= 500 \text{ mA g}^{-1}$ ),  $2 \text{ C}$  ( $= 1000 \text{ mA g}^{-1}$ ), and  $3 \text{ C}$  ( $= 1500 \text{ mA g}^{-1}$ ), the black P@C had higher reversible capacities of  $\sim 350$ ,  $\sim 310$ , and

$\sim 290 \text{ mAh g}^{-1}$  than those of the hard carbon anode ( $1 \text{ C}$ :  $\sim 65 \text{ mAh g}^{-1}$ ,  $2 \text{ C}$ :  $\sim 42 \text{ mAh g}^{-1}$ ,  $3 \text{ C}$ :  $\sim 33 \text{ mAh g}^{-1}$ ). Furthermore, the black P@C had excellent cycling ability above 200 cycles at the high rate of  $1 \text{ C}$ . The superior electrochemical performance of black P@C was attributed to the distinctive Na quasi-intercalation behavior between black P and NaP. Additionally, the preparation of a nanocomposite comprising nanocrystalline black P (approximately 5–10 nm size) in the conductive carbon black matrices contributed to the superior electrochemical performance of black P@C.

### 3. Conclusions

A Na quasi-intercalation concept in black P is developed to achieve superior P-based NIB anodes. Black P was synthesized by a simple solid-state reaction method using red P. Additionally, black P@C was prepared to optimize its electrochemical Na reversibility. The electrochemical two-step Na reaction pathway mechanism of sequential quasi-intercalation (NaP formation, at  $0.25 \text{ V}$ ) and conversion (Na<sub>3</sub>P formation, at  $0 \text{ V}$ ) of the black P to black P@C was demonstrated using various *ex situ* analytical

tools. Although black P@C showed poor cycling performance when using the conversion reaction within the voltage range of 0–2 V, it showed superior performance with highly reversible capacity, excellent cycling ability, and fast rate-capability when using the quasi-intercalation reaction between black P and NaP within the voltage range of 0.25–2 V. The new Na quasi-intercalation concept in black P discussed here will be readily applicable to advanced NIB anodes.

## Experimental Section

### Material synthesis

For the synthesis of black P, red P powder (99.9%, Dae-jung Chemicals & Metals, average particle size: 45 µm) was set into a steel vessel (volume: 80 cm<sup>3</sup>) with steel balls (20:1 ball-to-powder weight ratio). Thereafter, the steel vessel was tightly sealed in an Ar-filled glovebox to prevent oxidation of the sample. The solid-state process of BM was performed for 12 h using a SPEX 8000. To avoid a sudden temperature increase during the process, BM was paused for 30 min every hour. After the BM process was finished, the sample was left in the glovebox for sufficient time to stabilize (above 10 h). To obtain the carbon-modified composite of black P@C, the same BM process was carried out for 6 h on the powder mixture of the synthesized black P and carbon black (super P, Timcal), with the composition of 60:40 weight ratio.

### Material characterization

The samples of red P, black P, and black P@C were characterized using XRD (DMAX2500-PC, Rigaku, Cu-target), Raman spectroscopy (System 1000, Renishaw, laser with 514 nm wavelength), HRTEM (JEMARMF/JEOL, operating at 200 kV), 400 MHz solid-state NMR (Bruker, Avance2+, 31P solid echo MAS at 13 kHz), and EDX coupled with HRTEM. The size and morphology of sample particles were analyzed using a PSA (Mastersizer 2000) and SEM (JSM-6500, JEOL). The morphological changes, before and after the cycling of the black P and black P@C electrodes, were observed using SEM. The electrochemical Na reaction pathway mechanism of black P in black P@C during sodiation/desodiation was demonstrated using a combination of the ex situ analyzers of XRD, Raman spectroscopy, HRTEM, and EELS. Additionally, EI spectroscopy measurements were conducted using a ZIVE-MP2 A impedance analyzer (frequency range: 100 kHz–10 mHz) to compare the electrochemical resistance of red P, black P, and black P@C anodes before cycling at open circuit voltage.

### Electrochemical measurements

The electrodes of red P, black P, and black P@C consisted of 13.5 mm diameter and approximately 35 µm thick pellets containing the P-based powder materials, a conducting agent (carbon black, Denka), and a binder (polyvinyl alcohol-polyacrylic acid) with the composition of 70:10:20 weight ratio dissolved in deionized water on a Cu foil (25 µm thick). After coating, a vacuum drying process was conducted on the electrodes at 120 °C for 3 h and they were then pressed using a press roller. A separator (glass microfiber filter, GF/D) was sandwiched between the electrodes coated with the active materials of red P, black P, and black P@C (counter electrodes) and a Na metal disk (reference electrode). The average areal loading of the electrodes was maintained around 2.5 mg cm<sup>-2</sup>. An electrochemical coin-type cell tester (Maccor 4000, KOREA-THERMO-TECH) was used for all the electrochemical experi-

ments. An electrolyte of 0.7 M NaPF<sub>6</sub> salt in ethylene carbonate/diethyl carbonate (1:1 v/v, Panax STARLYTE) solvent with 5% fluoroethylene carbonate additive was used. All electrochemical half cells tested in two voltage ranges of 0–2 V (vs. Na<sup>+</sup>/Na) and 0.25–2 V (vs. Na<sup>+</sup>/Na) at a constant current density of 50 mA g<sup>-1</sup>, with the exception of the rate-capability tests. Differential dQ/dV plots were obtained by differentiating the capacity with respect to the voltage. The electrochemical method of constant capacity control was used to confirm the cycling performance at the constant capacity of 500 mA h g<sup>-1</sup> (sodiation: constant current density of 50 mA g<sup>-1</sup> for 10 h; desodiation: constant current density of 50 mA g<sup>-1</sup> to 2 V vs. Na<sup>+</sup>/Na).

### Acknowledgements

This work was supported by the National Research Foundation of Korea (NRF) grant, funded by the Korea Government (MSIP) (NRF-2018R1A2B6007112, NRF-2018R1A6A1A03025761). This research was also supported by the Grand Information Technology Research Center Program through the Institute of Information & Communications Technology and Planning & Evaluation (IITP) funded by the Ministry of Science and ICT (MSIT), Korea (IITP-2020-2020-0-01612).

### Conflict of Interest

The authors declare no conflict of interest.

**Keywords:** sodium-ion batteries • anode materials • black phosphorus • Na quasi-intercalation • reaction mechanism

- [1] a) N. Yabuuchi, K. Kubota, M. Dahbi, S. Komaba, *Chem. Rev.* **2014**, *114*, 11636–11682; b) M. D. Slater, D. Kim, E. Lee, C. S. Johnson, *Adv. Funct. Mater.* **2013**, *23*, 947–958; c) J.-Y. Hwang, S.-T. Myung, Y.-K. Sun, *Chem. Soc. Rev.* **2017**, *46*, 3529–3614; d) M. Dahbi, N. Yabuuchi, K. Kubota, K. Tokiwa, S. Komaba, *Phys. Chem. Chem. Phys.* **2014**, *16*, 15007–15028; e) H. Pan, Y.-S. Hu, L. Chen, *Energy Environ. Sci.* **2013**, *6*, 2338–2360.
- [2] a) Y. Wen, K. He, Y. Zhu, F. Han, Y. Xu, I. Matsuda, Y. Ishii, J. Cumings, C. Wang, *Nat. Commun.* **2014**, *5*, 4033; b) B. Jache, P. Adelhelm, *Angew. Chem. Int. Ed.* **2014**, *53*, 10169–10173; *Angew. Chem.* **2014**, *126*, 10333–10337.
- [3] a) D. A. Stevens, J. R. Dahn, *J. Electrochem. Soc.* **2001**, *148*, A803–A811; b) D. A. Stevens, J. R. Dahn, *J. Electrochem. Soc.* **2000**, *147*, 1271–1273; c) E. Irisarri, A. Ponrouch, M. R. Palacin, *J. Electrochem. Soc.* **2015**, *162*, A2476–A2482.
- [4] P.-C. Tsai, S.-C. Chung, S.-K. Lin, A. Yamada, *J. Mater. Chem. A* **2015**, *3*, 9763–9768.
- [5] Q. Fan, W. Zhang, J. Duan, K. Hong, L. Xue, Y. Huang, *Electrochim. Acta* **2015**, *174*, 970–977.
- [6] a) K.-H. Nam, G.-K. Sung, J.-H. Choi, J.-S. Youn, K.-J. Jeon, C.-M. Park, *J. Mater. Chem. A* **2019**, *7*, 3278–3288; b) K.-H. Nam, K.-J. Jeon, C.-M. Park, *Energy Storage Mater.* **2019**, *17*, 78–87.
- [7] a) Z. Li, J. Ding, D. Mitlin, *Acc. Chem. Res.* **2015**, *48*, 1657–1665; b) A.-R. Park, C.-M. Park, *ACS Nano* **2017**, *11*, 6074–6084; c) Y. Liu, N. Zhang, L. Jiao, Z. Tao, J. Chen, *Adv. Funct. Mater.* **2014**, *25*, 214–220.
- [8] a) J. Sun, G. Zheng, H.-W. Lee, N. Liu, H. Wang, H. Yao, W. Yang, Y. Cui, *Nano Lett.* **2014**, *14*, 4573–4580; b) T. Ramireddy, T. Xing, M. M. Rahman, Y. Chen, Q. Dutercq, D. Gunzelmann, A. M. Glushenkov, *J. Mater. Chem. A* **2015**, *3*, 5572–5584; c) H. Liu, L. Tao, Y. Zhang, C. Xie, P. Zhou, H. Liu, R. Chen, S. Wang, *ACS Appl. Mater. Interfaces* **2017**, *9*, 36849–36856; d) M. Dahbi, N. Yabuuchi, M. Fukunishi, K. Kubota, K. Chihara, K. Tokiwa, X.-F. Yu, H. Ushiyama, K. Yamashita, J.-Y. Son, et al., *Chem. Mater.* **2016**,

- [28] 1625–1635; e) K. P. S. S. Hembram, H. Jung, B. C. Yeo, S. J. Pai, S. Kim, K.-R. Lee, S. S. Han, *J. Phys. Chem. C* **2015**, *119*, 15041–15046; f) C.-M. Park, Y.-U. Kim, H.-J. Sohn, *Chem. Mater.* **2009**, *21*, 5566–5568; g) Z. Yu, J. Song, D. Wang, D. Wang, *Nano Energy* **2017**, *40*, 550–558; h) K.-H. Nam, C.-M. Park, *ACS Appl. Mater. Interfaces* **2020**, *12*, 15053–15062.
- [9] a) Y. Zu, X. Han, Y. Xu, Y. Liu, S. Zheng, K. Xu, L. Hu, C. Wang, *ACS Nano* **2013**, *7*, 6378–6386; b) M. He, K. Kravchyk, M. Walter, M. V. Kovalenko, *Nano Lett.* **2014**, *14*, 1255–1262; c) K.-H. Nam, C.-M. Park, *J. Power Sources* **2019**, *433*, 126639; d) G. Wang, X. Xiong, Z. Lin, C. Yang, Z. Lin, M. Liu, *Electrochim. Acta* **2017**, *242*, 159–164; e) Y.-H. Jang, C.-M. Park, *Mater. Today Energy* **2020**, *17*, 100470; f) J.-H. Choi, M.-H. Lee, H.-Y. Choi, C.-M. Park, S.-M. Lee, J.-H. Choi, *J. Appl. Electrochem.* **2018**, *49*, 207–216.
- [10] P. W. Bridgman, *J. Am. Chem. Soc.* **1914**, *36*, 1344–1363.
- [11] M. Ruck, D. Hoppe, B. Wahl, P. Simon, Y. Wang, G. Seifert, *Angew. Chem. Int. Ed.* **2005**, *44*, 7616–7619; *Angew. Chem.* **2005**, *117*, 7788–7792.
- [12] a) T. Nilges, M. Kersting, T. Pfeifer, *J. Solid State Chem.* **2008**, *181*, 1707–1711; b) A. Pfitzner, *Angew. Chem. Int. Ed.* **2006**, *45*, 699–700; c) A. Pfitzner, M. F. Bräu, J. Zweck, G. Brunklaus, H. Eckert, *Angew. Chem. Int. Ed.* **2004**, *43*, 4228–4231.
- [13] C.-M. Park, H.-J. Sohn, *Adv. Mater.* **2007**, *19*, 2465–2468.
- [14] Y. Yi, Z. Sun, J. Li, P. K. Chu, X. F. Yu, *Small Methods* **2019**, *3*, 1900165.
- [15] M. Batmunkh, M. Bat-Erdene, J. G. Shapter, *Adv. Energy Mater.* **2018**, *8*, 1701832.
- [16] Q. Jiang, L. Xu, N. Chen, H. Zhang, L. Dai, S. Wang, *Angew. Chem.* **2016**, *55*, 13849–13853.
- [17] A. Morita, *Appl. Phys. A* **1986**, *39*, 227–242.
- [18] R. Hultgren, N. S. Gingrich, B. E. Warren, *J. Chem. Phys.* **1935**, *3*, 351–355.
- [19] C.-M. Park, J.-H. Kim, H. Kim, H.-J. Sohn, *Chem. Soc. Rev.* **2010**, *39*, 3115–3141.
- [20] a) J. Sun, H.-W. Lee, M. Pasta, H. Yuan, G. Zheng, Y. Sun, Y. Li, Y. Cui, *Nat. Nanotechnol.* **2015**, *10*, 980–985; b) Y. Kim, Y. Park, A. Choi, N.-S. Choi, J. Kim, J. Lee, J. H. Ryu, S. M. Oh, K. T. Lee, *Adv. Mater.* **2013**, *25*, 3045–3049; c) W. Li, S. Hu, X. Luo, Z. Li, X. Sun, M. Li, F. Liu, Y. Yu, *Adv. Mater.* **2017**, *29*, 1605820; d) J. Qian, X. Wu, Y. Cao, X. Ai, H. Yang, J. Qian, X. Wu, Y. Cao, X. Ai, H. Yang, *Angew. Chem.* **2013**, *125*, 4731–4734; e) Y. Zhu, Y. Wen, X. Fan, T. Gao, F. Han, C. Luo, S.-C. Liou, C. Wang, *ACS Nano* **2015**, *9*, 3254–3264; f) W.-J. Li, S.-L. Chou, J.-Z. Wang, H.-K. Liu, S.-X. Dou, *Nano Lett.* **2013**, *13*, 5480–5484.
- [21] M. Saifuddin, S. Kim, A. Azia, K. S. Kim, *Appl. Sci.* **2019**, *9*, 4897.
- [22] Y. Lu, P. Zhou, K. Lei, Q. Zhao, Z. Tao, J. Chen, *Adv. Energy Mater.* **2016**, *7*, 1601973.
- [23] a) W. Xia, Q. Zhang, F. Xu, H. Ma, J. Chen, K. Qasim, B. Ge, C. Zhu, L. Sun, *J. Phys. Chem. C* **2016**, *120*, 5861–5868; b) G. Nicotra, A. Politano, A. M. Mio, I. Deretzi, J. Hu, Z. Q. Mao, J. Wei, A. L. Magna, C. Spinella, *Phys. Status Solidi B* **2016**, *253*, 2509–2514.
- [24] a) C.-M. Park, *J. Solid State Chem.* **2015**, *20*, 517–523; b) C.-M. Park, H.-J. Sohn, *Adv. Mater.* **2010**, *22*, 47–52.

Manuscript received: August 7, 2020

Revised manuscript received: September 19, 2020

Accepted manuscript online: September 22, 2020

Version of record online: October 12, 2020